Chapter 9
Microstructured Optical Fiber-Based Plasmonic Sensors

Ahmmed A. Rifat, Md. Rabiul Hasan, Rajib Ahmed and Andrey E. Miroshnichenko

Abstract Surface plasmon resonance (SPR) is a considerably growing optical sensing approach which has been employed in wide range of applications including medical diagnostics, biological and chemical analyte detection, environmental monitoring, and food safety to security. SPR sensing technique shows high sensitive nature due to small change of sample refractive index, compared to other optical sensing techniques. Recently, microstructured optical fiber-based plasmonic sensors have shown great development due to its compact structure and light controlling capabilities in unprecedented ways. The goal of this chapter is to (1) describe the principle operation of plasmonic sensors, (2) discuss the optical properties of plasmonic materials, (3) compare and contrast the different types of microstructured optical fiber-based plasmonic sensors, and (4) highlight the main challenges of microstructured plasmonic sensors and possible solutions.

Keywords Surface plasmon resonance · Microstructured optical fiber Optical fiber sensors · Optical sensing and sensors

A. A. Rifat (✉) · A. E. Miroshnichenko
Nonlinear Physics Centre, Research School of Physics & Engineering, Australian National University, Acton, ACT 2601, Australia
e-mail: RifatAhmmed.Aoni@anu.edu.au

Md. Rabiul Hasan
Department of Electronics & Telecommunication Engineering, Rajshahi University of Engineering & Technology, Rajshahi 6204, Bangladesh

R. Ahmed
Nanotechnology Laboratory, School of Engineering, University of Birmingham, Birmingham B15 2TT, UK

A. E. Miroshnichenko
School of Engineering and Information Technology, University of New South Wales, Canberra, ACT 2600, Australia

© Springer International Publishing AG, part of Springer Nature 2019

M. F. O. Hameed and S. Obayya (eds.), *Computational Photonic Sensors*, https://doi.org/10.1007/978-3-319-76556-3_9

9.1 Introduction

Over the last three decades, surface plasmon resonance (SPR) has been considered as the key technology for numerous sensing applications. SPR sensors are powerful and effective tool that have been widely used in biosensing [1, 2], bioimaging [3], chemical detection [4–7], water testing [8], aqueous sample detection [9, 10], food safely [11, 12], environmental monitoring [13], biological analyte detection [4, 14], and gas detections [15, 16] (Fig. 9.1). Due to ongoing advancement of SPR technology, it has been also employed in optoelectronic devices such as optical tunable filters [17, 18], optical modulators [19, 20], film thickness monitoring [21, 22], and SPR imaging [23, 24]. Additionally, SPR technology enables integration of nanoelectronic and nanophotonic components with the aim to obtain ultra-compact optoelectronic devices [25, 26]. In 1907, the origin of SPR was first theoretically formulated by Zenneck [27], where it was demonstrated that surface electromagnetic

Fig. 9.1 Applications of surface plasmon resonance sensors

waves can be observed at the boundary of two mediums when one medium is lossless and another medium is either lossy dielectric or metal. In 1909, Sommerfeld first observed that surface waves are fast and attenuate exponentially with height above the interface [28]. The actual progress of SPR was carried out by Ritchie. In 1957, physical existence of the surface waves at the metal–dielectric interface was demonstrated [29].

Conventional prism-coupling-based SPR sensors are classified into two categories: Kretschmann [30] and Otto configurations [31]. The operating principle of both these sensors is attenuated total reflection (ATR). Although Kretschmann-based configuration SPR sensors are widely employed due to their excellent sensing performances, they suffer from several limitations. In general, these SPR sensors are bulky and made with moving optical and mechanical parts. As a result, they are not portable and cannot be used for remote sensing applications [6]. Moreover, practical implementation of spectral-based measurement is costly and scope for scaling down the sensor size is limited. To effectively overcome such potential difficulties, optical fiber-based SPRs are introduced [32–35]. Optical fibers are simple and have lightweight. Moreover, due to flexible design of the optical fiber it is possible to reduce the sensor size to a great extent, which can be potentially used for remote sensing applications [35]. Optical fiber-based SPR sensors provide higher dynamic range for detection and high resolution; however, they are applicable only for narrow acceptance angles [36]. Several optical fiber SPR sensors have been reported by both theoretical and experimental investigations [32–35].

Recently, photonic crystal fiber (PCF)-based SPR sensors have been extensively studied due to their unusual and appealing optical characteristics over the conventional optical fiber [37–56]. The optical properties of the PCF (such as confinement loss, single-mode propagation, birefringence, etc.) can be easily tailored, which eventually enable to control the performance of the sensor [57–60]. By changing the structural parameters such as pitch, air hole dimension, and number of air hole rings, it is possible to operate the sensor at the optimum condition [42, 50]. Current fabrication technologies are well-developed that permit practical realization of the PCF sensors. However, experimental characterizations of PCF-based SPR sensors are not matured enough to date. Therefore, existing PCF sensors are mostly demonstrated by numerical analysis. Finite element method (FEM) is a powerful numerical technique, which is widely adopted to characterize the optical properties of PCF sensors. Besides, spectral (wavelength)- and intensity (amplitude or phase)-based numerical calculations are used to evaluate the sensing performance of the PCF SPR sensors [61].

In this chapter, current developments of SPR sensors are introduced and discussed. We will mainly focus on the review of the PCF-based SPR sensors and their potential applications in medical diagnostics and industrial settings. First, fundamentals of SPR technology and optical properties of several plasmonic materials (silver, copper, aluminum, gold, graphene, and niobium) are discussed. Then, we introduce several optical fiber-based SPR sensors and discuss how it overcomes the major limitations of prism-based SPR sensors. Later, recent advances of existing

PCF-based SPR sensors are discussed, which consist of comparisons among several PCF structures in terms of sensitivity, resolution, and fabrication feasibility. Finally, research gaps of this field are addressed and potential future detections to overcome them are discussed.

9.2 Fundamentals of Surface Plasmon Resonance

Inside a conductor (metal), there are lots of free electrons and an assembly of the electrons can be considered as plasma excitations. At the same time, there are equal numbers of positive charged ions from lattice so the total charge density in the conductor is zero. If an external field is applied, the electrons will be moving toward the positive region, and at the same time, the positive ion will be moving as opposite to the electrons. Due to such transport, a longitudinal oscillation will be introduced in the conductor which is known as surface plasmons (SPs) [62]. To support the SPs, a conductor and dielectric interface is required. In general, a metal and dielectric interface is used to support the surface plasmon oscillations. Due to these oscillations and a certain resonance condition, surface plasmon waves (SPWs) are generated that propagates along the metal–dielectric surface. Such SPs support only transverse magnetic (TM)-polarized electromagnetic field since there is no solution of Maxwell's equations for transverse electric (TE)-polarized case. Therefore, for SPW only the TM-polarized electric field exists. This wave is decayed exponentially in the metal. This SPW is characterized by the propagation constant as [63]

$$\beta = \frac{\omega}{c}\sqrt{\frac{\varepsilon_{\mathrm{M}}\varepsilon_{\mathrm{D}}}{\varepsilon_{\mathrm{M}}+\varepsilon_{\mathrm{D}}}} \tag{9.1}$$

where ω is the angular frequency, c is the speed of light in vacuum, and ε_{M} and ε_{D} are the dielectric permittivities of metal and dielectric medium, respectively. According to the above equations, property of the SPW is dependent on the property of two materials, i.e., the metal and the dielectric media.

To create the surface plasmon oscillation, it is required to excite the electrons in the conductor. Therefore, imposing the light (EM field) is necessary on the surface. The electrical permittivity for the conductor (metal) is negative, and the electrical permittivity for the dielectric is positive. In the dielectric medium, the propagation constant (maximum) can be written as [64]

$$\beta = \frac{\omega}{c}\sqrt{\varepsilon_S} \tag{9.2}$$

where ε_{S} is the dielectric permittivity of sensing medium. It is stated that the propagation constant for surface plasmon wave is higher than the propagation constant of light in the dielectric medium. As a result, surface plasmon cannot be

excited with the normal light; it requires the light with extra momentum or energy with the same polarization state as the SPW. Moreover, the propagation constant should be matched with the surface plasmon wave.

PCF-based SPR sensors operate based on the guided evanescent field. When the light propagates through the core by the mechanism of total internal reflection (TIR), then a part of the electromagnetic field that propagates from the cladding is called the evanescent field. In PCF SPR sensor structure, evanescent field penetrates through the cladding region and hits on the plasmonic metal surface which excites the free electrons from the metallic surface. When the frequency of the incident photon and the frequency of the free electrons are matched, the electrons start to resonate and at this condition SPW is generated on the metal–dielectric interface. At the resonance condition, a sharp loss peak appears which is very sensitive to the small refractive index (RI) variation of the dielectric medium. Mathematically, resonance will occur when the real effective refractive index (n_{eff}) of core-guided mode and surface plasmon polariton (SPP) mode value are equal. At the resonance condition, maximum energy transfers from the core-guided mode to the SPP mode [42]. Due to the change of refractive index of the dielectric media (sample analyte), n_{eff} of SPP will change resulting in a loss peak and the resonant wavelength shift. This indicates the phase-matching wavelength changes with the change of sample/analyte refractive index. Unknown sample could be detected by observing the variation of loss peak due to the change of analyte RI [61].

9.3 Optical Properties of Plasmonic Materials

PCF-based SPR sensors mostly use gold, copper, silver, and aluminum as the active plasmonic materials [65]. From the optical point of view, silver can be regarded as one of the potential candidates for plasmonic material [66]. The positive attributes of silver are no interband transition in the visible wavelength spectrum, low optical damping, narrow resonance peak, and a plasma wavelength (137 nm) deep in the ultraviolet wavelength range [67]. However, in the presence of aqueous solution it creates brittle oxide layers, which obstructs its widespread applications as plasmonic sensors [68]. Although such formation of oxide layer can be strongly prevented by depositing bimetallic layer on the top of the silver [69, 70], this additional layer will deteriorate the performance of the sensor. Compared to silver, aluminum has not attracted much attention due to its high optical damping, oxidation issue, and interband transition loss [71].

Current SPR sensors mostly rely on gold as the plasmonic material due to several advantages. Gold is chemically inert, biocompatible, long-term stable, and easy to structure. Moreover, gold does not suffer from oxidation issue [67, 72]. However, it has slightly higher optical damping and has broadened resonance wavelength peak leading to false positive analyte detection [44]. Copper is another potential plasmonic material possessing almost same optical damping and interband transition as gold in the wavelength range of 600–750 nm [73]. Unfortunately,

copper is also prone to oxidation. Recently, graphene is used on the top of the copper or silver in order to prevent the oxidation issue [74, 75]. Graphene is chemically inert and mechanically strong that keeps it isolated from contacting with aqueous solution [76]. Copper–graphene- [74] and silver–graphene [42]-based PCF SPR sensors possess long-term stability and stable performance. These widely used plasmonic materials are unfeasible when the thickness of the films is scaled down below ten nanometers because it leads to discontinuous film [77, 78]. Moreover, conventional plasmonic materials show poor adhesion strength with silica glass that requires additional adhesion layer. Employing such adhesion layer causes more damping loss; therefore, the performance of the sensor reduces significantly [66].

Niobium is a novel plasmonic material having strong chemical resistivity and high mechanical stability [79]. The adhesion strength of niobium film with silica glass is so strong that does not require an adhesion layer. Moreover, in contrast to gold, niobium provides continuous film when the thickness of the film falls below ten nanometers [80, 81]. Furthermore, after depositing niobium film on the silica surface, several atomic protection layers are naturally formed [82]. Although this layer has no optical functionality, it prevents the film from external perturbations of the environment. Recently, indium tin oxide (ITO)-based SPR sensors have achieved increased attention due to low bulk plasma frequency [43]. Moreover, its optical damping is almost same as gold and silver [83, 84].

9.4 Fiber Optic-Based Plasmonic Sensors

In contrast to prism-coupling SPR sensors, fiber optic-based SPR sensors provide several advantages such as simple and flexible design, ease of miniaturization, and capability for remote sensing and vivo measurements [51]. The prim-coupling configuration of the conventional SPR system is replaced by the core, where light is guided by the total internal reflection (TIR) mechanism. In fiber optic SPR sensors, certain portion of the silica cladding is removed and a metal layer is deposited on it. Later on, the metal layer is coated with a dielectric sensing layer. A light source is used to launch the light from an end of the fiber, which propagates by TIR mechanism. The generated evanescent field creates SPs at the fiber core–metal interface.

In general, fiber optic plasmonic sensors are based on either transmission or reflection properties of the guided light [51]. Fiber optic sensors based on transmission probe consist of plasmonic metal and immobilized ligand to detect the unknown analytes [56, 85]. On the other hand, sensors based on reflection probe use a mirror to reflect backlight to the fiber. Based on the transmission probe, several fiber optic plasmonic sensors have been explored in the literature, where plasmonic materials are placed on the etched cladding section. They include single-mode fibers (SMFs) [86], multi-mode fibers (MMFs) [87], wagon wheel fiber [88], U-shaped fiber [89], D-shaped fiber [90], tapered fiber [66, 91, 92], and

Bragg grating fibers [93]. Recently, side-polished single-mode optical fiber-based SPR sensor has been demonstrated for simple and cost-effective biochemical detections (see Fig. 9.2a(i)) [94]. With varying refractive index from 1.32 to 1.40, the highest sensitivity of 4365.5 nm/RIU and figure of merit (FOM) of 51.61 RIU^{-1} were reported (Fig. 9.2a(ii)). Niobium nanofilm was deposited on the tapered optical fiber in order to observe a dielectric-loaded niobium surface plasmon excitation (see Fig. 9.2b) [66]. The cross-sectional view of the sensor is shown in Fig. 9.2b(i). The cross-sectional view of the taper fiber optic sensor with different materials is shown in Fig. 9.2b(ii). Poynting vector distributions of dielectric and

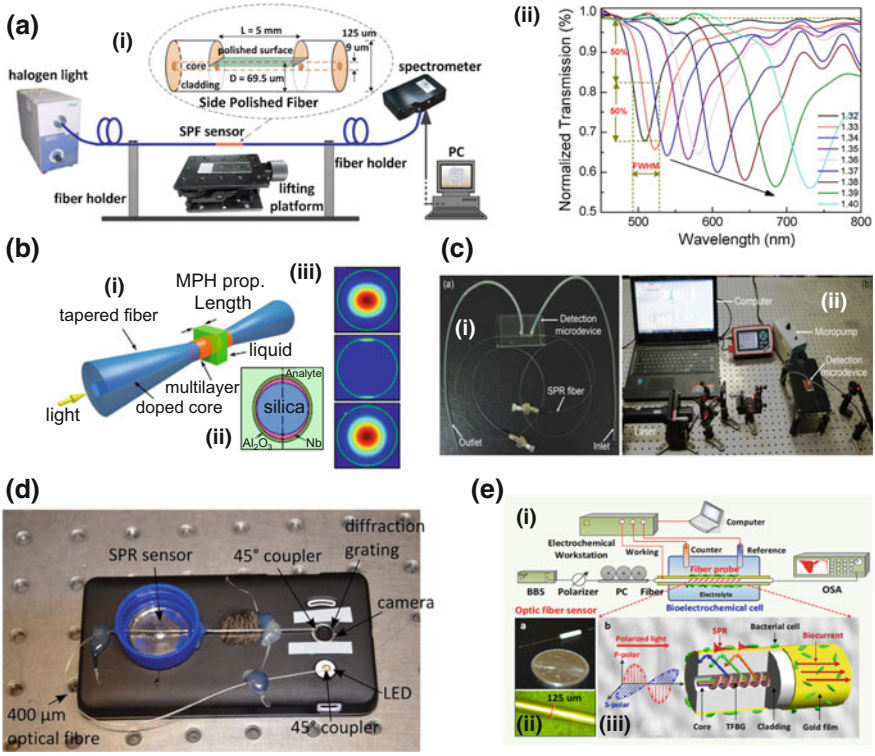

Fig. 9.2 Fiber optic-based SPR sensors. **a(i)** Schematic diagram to test the refractive index using side-polished D-shaped fiber and **(ii)** normalized transmission spectra due to the variation of analyte refractive index from 1.32 to 1.40 [94]. **b(i)** Schematic diagram of the plasmonic taper fiber with the multilayer structure, **(ii)** cross-sectional view showing different materials of the sensor, and **(iii)** Poynting vector distribution of the fundamental and SPP mode. Reprinted with permission from Macmillan Publishers Ltd. [66]. **c(i)** Microdevice installed with the SPR fiber sensor head and **(ii)** the experimental setup for the detection of polymerase chain reaction amplification with SPR fiber sensor system. Reprinted with permission from Elsevier B.V. [95]. **d** Smartphone-based fiber optic SPR sensor for pregnancy test. Reprinted with permission from Optical Society of America [96]. **e(i)** Schematic of the plasmonic fiber optic sensing system for in situ biofilm monitoring, **(ii)** SEM image of the gold-coated optic fiber sensor, and **(iii)** the zoomed configuration of the gold-coated sensor probe. Reprinted with permission from the American Chemical Society [97]

SPP mode are shown in Fig. 9.2b(iii). The proposed plasmonic sensor shows low modal attenuation of 4 dB/mm and refractive index sensitivity of 15 μm/mm with analyte index of 1.42. A SPR optical fiber sensor for the detection of polymerase chain reaction amplification has been reported by Nguyen et al. [95] using bimetallic (Ag/Al) coating (see Fig. 9.2c). A smartphone-based optical fiber sensor has been reported by Bremer and Roth [96] for concentration measurements on aqueous solutions and pregnancy testing (see Fig. 9.2d). A sensitivity of 5.96×10^{-4} RIU/pixel was obtained in the sensing range between 1.33 and 1.36. Recently, electrochemical SPR fiber optic sensor has been proposed for in situ monitoring of electroactive biofilms (see Fig. 9.2e) [97].

9.5 Photonic Crystal Fiber-Based Plasmonic Sensors

PCF is a new class of optical fiber that consists of a core and cladding with periodic arrangement of air hole arrays [98]. Such periodic arrangement of the air holes controls the propagation characteristics of the PCFs. The light guiding mechanism in PCF is modified TIR and photonic band gap [99, 100]. In contrast to conventional optical fiber, PCF-based SPR sensors offer several advantages. By varying the air hole dimension and number of rings in a PCF, it is possible to control the guiding properties of the PCF. In general, PCFs are compact and can be fabricated in micron scale. Unlike prism-coupling and conventional optical fiber-based SPR sensors, PCF-based SPR sensors provide potential platform for downscaling the sensor size. Moreover, the unique features of PCFs have opened a new window for realizing nanosensors. Several cladding structures including hexagonal, octagonal, circular, square, and hybrid can be used to modify the evanescent field; thereby, it is possible to obtain the optimum sensing performance [101]. Furthermore, single-mode propagation can be obtained by properly choosing the core–cladding diameter. Single-mode guidance provides sharp resonance peak that increases the sensitivity of a sensor [102]. The detection accuracy and sensitivity of the PCF SPR sensors can be optimized by changing the structural parameters such as pitch and air hole dimensions. Besides, sensor length can be extended by setting the fiber parameters in such a way that exhibits minimum propagation loss. In practice, depositing the metal layer on the PCF is a difficult task. The existing fabrication technologies can be employed to deposit the metal layer inside or outside of the PCFs. Based on the metal deposition on the PCF, SPR sensors are classified into two major categories. They are internally and externally metal-coated SPR sensors.

9.5.1 Internally Metal-Coated PCF SPR Sensors

The internally metal-coated PCF SPR sensors are based on the deposition of metal layer on the inner air hole(s), which are filled by the analyte. To date, several PCF

structures have been explored where metal layer is placed inside the PCF and liquid analytes are selectively filled into the inner air hole(s) [39, 41–43, 103–107]. Very recently, diamond ring fiber (DRF)-based SPR sensor has been proposed (see Fig. 9.3a) by numerical investigations [108]. This is an all-silica fiber containing a ring capillary with thickness of 0.94 μm. The diameter of the core is 3.23 μm. A thin layer of gold is deposited on the inner wall of the capillary. The DRF contains two large cavities, which simplify the metal coating process. Moreover, this sensor does not require selective infiltration of the liquid sample. The evanescent field created from the fundamental core-guided mode reaches at the metal boundary, which resembles free electrons from its surface. Due to the interaction of emitted electrons and evanescent field, SPW is generated that propagates along the metal–dielectric surface. The electric field distribution of the fundamental core-guided mode and SPP mode is shown in Fig. 9.3b. When the effective index of core-guided mode and SPP mode is equal, a phase-matching condition occurs at a particular wavelength known as the resonance wavelength. Under this condition, confinement loss peak is observed at the resonance wavelength (see Fig. 9.3c) resulting in maximum power transfer from the core-guided mode to the SPP mode. The confinement loss can be computed from the following equation $\alpha(\text{dB/cm}) = 8.686 \times (2\pi/\lambda)\ \text{Im}(n_{\text{eff}}) \times 10^4$, where $\text{Im}(n_{\text{eff}})$ is the

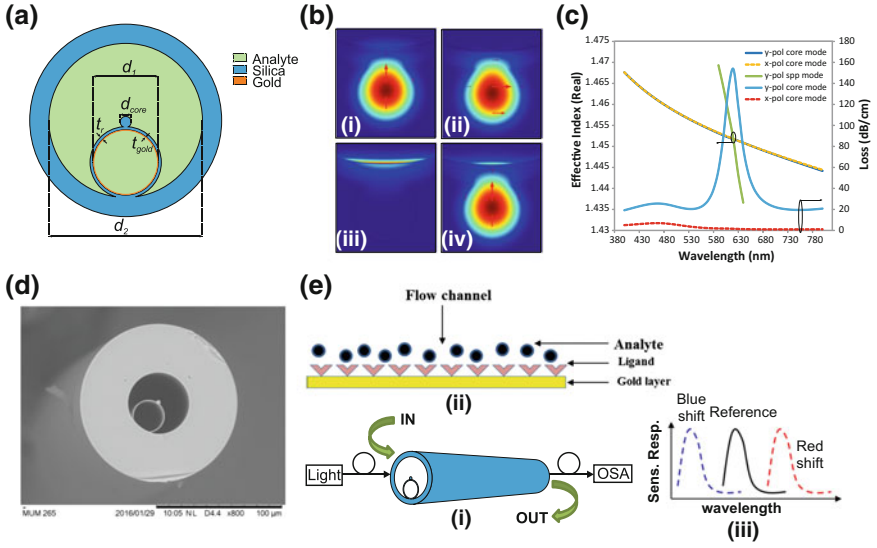

Fig. 9.3 **a** Cross-sectional view of the DRF showing different materials used in the structure. **b** Fundamental mode field distributions of the **(i)** *y*-polarized core mode, **(ii)** *x*-polarized core mode, **(iii)** *y*-polarized SPP mode at 580 nm, and **(iv)** *y*-polarized core mode at 620 nm. **c** Dispersion relation between core-guided mode and SPP mode at analyte refractive index of 1.33. **d** SEM image of the DRF. **e(i)** Generalized sensing setup using the DRF, **(ii)** analyte flow mechanism for DRF-based sensor, and **(iii)** sensing response observed from the computer. Reprinted with permission from Springer [108]

imaginary part of the effective mode index. The proposed DRF is fabricated using the stack-and-draw method, and the scanning electron microscope (SEM) image is shown in Fig. 9.3d. Figure 9.3e(i)–(ii) shows the generalized experimental setup that can be implemented based on the DRF–SPR sensor. Broadband supercontinuum laser source can be lunched to the SMF. The propagating light can be coupled to the DRF by using the butt-coupling technique. Due to the interaction of the evanescent field with the ligand, the effective index of SPP mode expected to be changed. As a result, blue or red shift will occur as shown in the sensing response curve (see Fig. 9.3e(iii)). The output light can be coupled with the optical spectrum analyzer (OSA), and it can be processed using computer.

The performance of SPR sensors can be analyzed using wavelength sensitivity (spectral-based analysis), amplitude sensitivity (intensity-based analysis), and sensor resolution. The wavelength sensitivity of a sensor can be expressed as [109]

$$S_\lambda(\mathrm{nm/RIU}) = \Delta\lambda_{\mathrm{peak}}/\Delta n_{\mathrm{a}} \tag{9.3}$$

where $\Delta\lambda_{\mathrm{peak}}$ is the peak wavelength shift due to any change of analyte RI and Δn_a is the change of the two successive analyte RIs. On the other hand, amplitude sensitivity can be manipulated by the following equation [45, 109]

$$S_A(\mathrm{RIU}^{-1}) = -\frac{1}{\alpha(\lambda, n_{\mathrm{a}})}\frac{\partial\alpha(\lambda, n_{\mathrm{a}})}{\partial n_{\mathrm{a}}} \tag{9.4}$$

where $\alpha(\lambda, n_a)$ is the confinement loss at refractive index of n_a and $\partial\alpha(\lambda, n_a)$ is the confinement loss difference due to two adjacent analyte RIs. In the sensing range between 1.33 and 1.39, the DRF-based SPR sensor shows maximum wavelength and amplitude sensitivity of 6000 nm/RIU and 508 RIU^{-1}, respectively. Assuming instrumental resolution of 0.1 nm and avoiding practical noise influence, the calculated wavelength resolution is 1.67×10^{-5} RIU. Besides, amplitude resolution of 1.97×10^{-5} RIU is reported, while it is assumed that 1% transmitted intensity can be detected by the sensor. A liquid core PCF with two selectively analyte-filled channels has been demonstrated, where graphene–silver coating was used to improve the sensing performance (see Fig. 9.4a(i)) [42]. The phase-matching conditions are shown in Fig. 9.4a(ii) for analyte index of 1.47 and 1.49, respectively. It was reported that at optimum design parameters it is possible to obtain maximum wavelength and amplitude sensitivity of 3000 nm/RIU and 418 RIU^{-1}, respectively. The corresponding sensor resolutions are 3.33×10^{-5} and 2.4×10^{-5} RIU, respectively. Moreover, another PCF SPR sensor has been proposed by Yang et al. using graphene–silver bimetallic configuration [110]. In this sensor, two rings hexagonal PCF was considered, where six air holes of the second ring were selectively infiltrated by the analyte. In the sensing range between 1.33 and 1.34, maximum wavelength and amplitude sensitivity of 2520 nm/RIU and 72.47 RIU^{-1}, respectively. The selectively analyte-filled PCF SPR sensor proposed by Fan et al. shows average wavelength sensitivity of 7040 and 7017 nm/RIU using gold and silver as the plasmonic material, respectively [105]. Moreover, the

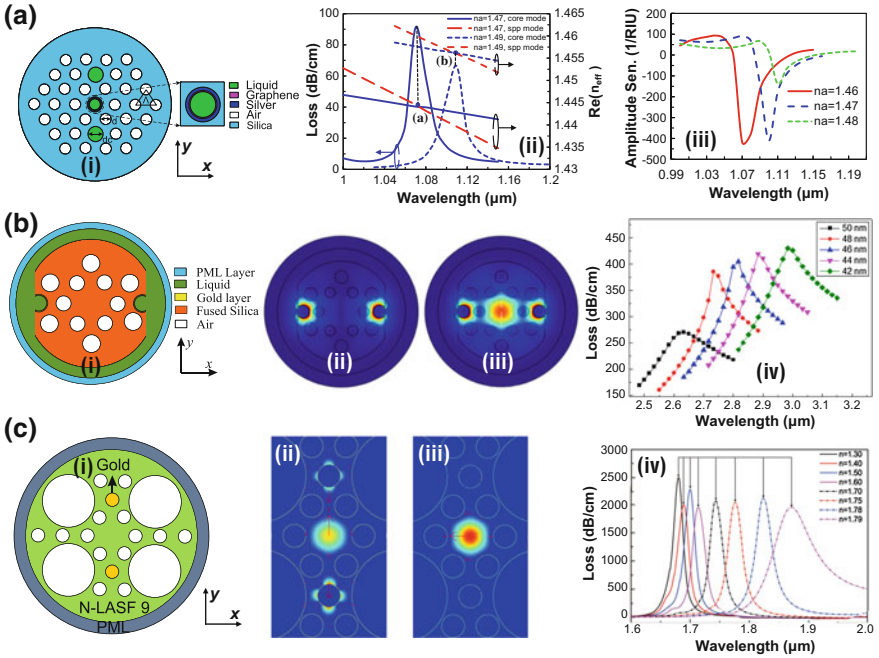

Fig. 9.4 Internally metal-coated PCF SPR sensors. **a(i)** Cross-sectional view of the liquid core PCF with selectively analyte-filled sensor, **(ii)** dispersion relation between core-guided mode and SPP mode at analyte refractive index of 1.47 and 1.49, and **(iii)** amplitude sensitivity as a function of wavelength for analyte refractive index of 1.46, 1.47, and 1.48. Reprinted with permission from MDPI AG [42]. **b(i)** Cross-sectional view of the open ring PCF sensor, **(ii)** optical field distribution of the plasmonic mode, **(iii)** optical field distribution of the fundamental core-guided mode, and **(iv)** loss spectra for the variation of gold layer thickness. Reprinted with permission from Optical Society of America [112]. **c(i)** Cross-sectional view of the gold nanowire-based PCF sensor, **(ii)** optical field distribution of the plasmonic mode, **(iii)** optical field distribution of the fundamental core-guided mode, and **(iv)** loss spectra for the variation of analyte refractive index [113]

reported figure of merit (FOM) for gold and silver was 73.8 and 5.9 RIU^{-1} at analyte refractive index of 1.40. Very recently, multi-coating PCF SPR sensor proposed by Li et al. employs tantalum pentoxide (Ta_2O_5) on gold in order to further improve the sensitivity [111]. The proposed sensor shows average wavelength sensitivity of 9180 nm/RIU and maximum amplitude sensitivity of 1739.26 RIU^{-1}, respectively.

In practice, it is a difficult task to selectively filling the air holes with the analyte. To overcome this limitation, PCF SPR sensor having open rings channels was proposed [112]. The analyte can be injected into the channels automatically, and size of the open rings can be controlled according to the molecular concentrations of the analyte. The hollow-core open ring PCF sensor operates in the mid-infrared region and can be used to detect low refractive indices between 1.23 and 1.29 (see Fig. 9.4b(i)) [112]. Mode field distribution of the core-guided mode, SPP mode,

and loss variations due to analyte index change is shown in Fig. 9.4b(ii)–(iii). With optimum design parameters, average wavelength sensitivity of 5500 nm/RIU and maximum amplitude sensitivity of 333.8 RIU^{-1} were reported. In practice, disposition of metal on several air holes maintaining uniform thickness is unfeasible from the fabrication point of view. Nanowire-based PCF sensors provide viable way to eliminate those issues. To date, several PCF SPR sensors have been realized using silver and gold nanowires [114–116]. Recently, silver nanowire-based PCF SPR glucose sensor has been proposed showing high average wavelength sensitivity of 19009.17 nm/RIU and amplitude sensitivity of 513.68 RIU^{-1} [52]. Gold nanowire-based PCF SPR sensor (see Fig. 9.4c(i)) proposed by An et al. can be used to detect analyte refractive index from 1.30 to 1.79 [113]. It contains four large air holes that make it easier to inject the analyte. The electric field distributions of the core-guided mode, SPP mode, and confinement loss for different analyte refractive index are shown in Fig. 9.4c(ii)–(iii). In the sensing range between 1.30 and 1.63, average wavelength sensitivity of 100 nm/RIU and in the sensing range between 1.63 and 1.79, average wavelength sensitivity of 3233 nm/RIU were reported. Very recently, hollow-core silver nanowire-based PCF SPR sensor has been proposed having large detection range from 1.33 to 1.50 [117]. The proposed sensor shows maximum wavelength sensitivity of 1800 nm/RIU when analyte index is varied from 1.33 to 1.34. Nanowire-based PCF can be fabricated by implementing the Taylor wire method [90]. Table 9.1 shows the performance comparison among existing internally metal-coated PCF SPR sensors.

9.5.2 Externally Metal-Coated PCF SPR Sensors

To potentially overcome the major limitations such as the requirements for selective infiltration of liquids, metal coating of several air holes, and complex fabrication, externally metal-coated PCF SPR sensors have been proposed. Unlike internally metal-coated PCF sensors, plasmonic materials are deposited on the outer surface of the PCF facilitating straightforward sensing mechanism. Based on the structural configurations, external metal-coated PCF SPR sensors are generally three types: slotted PCF sensors, D-shaped PCF sensors, and improved external PCF sensors.

9.5.2.1 Slotted PCF SPR Sensors

Slotted PCF SPR sensors are mainly developed in order to detect multiple analytes. Various structural configurations have been proposed in the literature for this purpose [50, 118–121]. The PCF-based SPR sensor proposed by Hassani et al. was used for the detection of biolayer thickness (see Fig. 9.5a(i)) [119]. Plasmonic gold and biolayer were deposited outside the PCF surface. Six smaller air holes are placed near the gold surface to control the coupling strength between core-guided mode and SPP mode. The central air hole was used to maintain the phase-matching

Table 9.1 Performance comparison of the internally metal-coated PCF SPR sensors

References	Characteristics	RI range	Interrogation type	Sensitivity	Resolution (RIU)
[42]	Graphene–silver deposited core with selective analyte channels	1.46–1.49	Wavelength	3000 nm/RIU	3.33×10^{-5}
			Amplitude	418 RIU^{-1}	2.4×10^{-5}
[43]	Polymer PCF coated with conducting metal oxide	1.33–1.35	Wavelength	2000 nm/RIU	5×10^{-5}
			Amplitude	80 RIU^{-1}	12×10^{-5}
[48]	Selectively filled silver nanowires	1.33–1.335	Wavelength	N/A	4.5×10^{-5}
			Amplitude	203 RIU^{-1}	4.9×10^{-5}
[103]	Multi-hole single-mode PCF	1.33–1.35	Wavelength	2000 nm/RIU	5×10^{-5}
			Amplitude	370 RIU^{-1}	2.7×10^{-5}
[104]	Selectively gold coating with analyte-filled core PCF	1.46–1.485	Wavelength	2280 nm/RIU	N/A
			Wavelength	−4354.3 nm/RIU	N/A
[105]	Analyte-filled PCF with selective coating	1.40–1.42	Wavelength	7040 nm/RIU	N/A
			Wavelength	7017 nm/RIU	N/A
[107]	PCF with large size microfluidic channels	1.33–1.39	Wavelength	2000 nm/RIU	5×10^{-6}
			Amplitude	300 RIU^{-1}	3.3×10^{-5}
[108]	Diamond ring PCF	1.33–1.39	Wavelength	6000 nm/RIU	1.67×10^{-5}
			Amplitude	508 RIU^{-1}	1.97×10^{-5}
[110]	Graphene–silver bimetallic layer PCF	1.33–1.35	Wavelength	2520 nm/RIU	3.97×10^{-5}
			Amplitude	72.47 RIU^{-1}	N/A
[111]	Analyte-filled multi-coated PCF	1.40–1.44	Wavelength	9180 nm/RIU	1.09×10^{-5}
			Amplitude	1739.26 RIU^{-1}	5.75×10^{-6}
[112]	Open ring channels PCF	1.23–1.29	Wavelength	5500 nm/RIU	7.69×10^{-6}
			Amplitude	333.8 RIU^{-1}	N/A
[113]	Gold nanowires with large size channels	1.30–1.79	Wavelength	3233 nm/RIU	3.09×10^{-5}
			Amplitude	N/A	N/A
[116]	Hollow-core PCF with silver-filled nanowire	1.10–1.60	Wavelength	14,240 nm/RIU	N/A
			Amplitude	N/A	N/A

characteristics. The mode field distributions of the core-guided mode and SPP mode at 575 nm are shown in Fig. 9.5a(ii)–(iii). It is demonstrated that with gold layer thickness of 50 nm, a wavelength shift of 23 nm can be obtained when biolayer thickness is increased from 0 to 10 nm (see Fig. 9.5a(iv)). Recently, a multi-channel PCF-based sensor has been proposed, where plasmonic silver is coated with the gold (see Fig. 9.5b(i)) [122]. The loss spectrum of the quasi-TM and TM fundamental core modes for analyte refractive index of 1.33 and 1.34 are shown in Fig. 9.5b(ii)–(iii). The proposed bimetallic SPR sensor shows maximum wavelength sensitivity of 4750 nm/RIU and 4300 nm/RIU for quasi-TM and TM fundamental core mode, respectively. The major limitation of this sensor is the high confinement loss, which potentially limits its length. In general, the signal strength

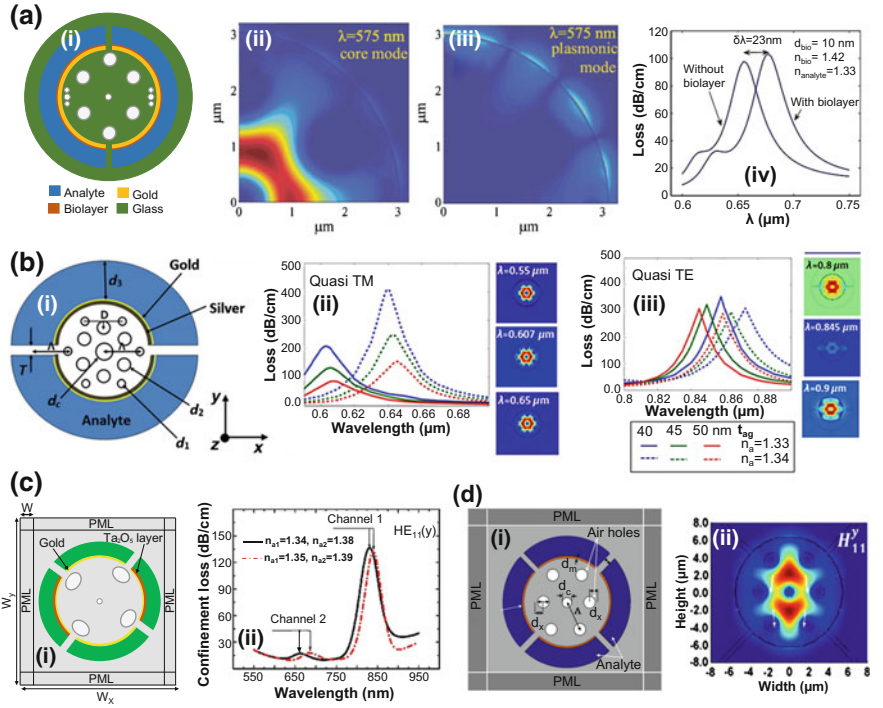

Fig. 9.5 Slotted PCF SPR sensors. **a(i)** Cross-sectional view of the slotted PCF sensor with the air hole defects in the near vicinity of the gold layers, **(ii)** optical field distribution of the fundamental mode, **(iii)** optical field distribution of the SPP mode, and **(iv)** effect of inserting biolayer on the loss spectra. Reprinted with permission from Optical Society of America [119]. **b(i)** Cross-sectional view of the bimetallic-slotted PCF sensor, **(ii)** loss spectra for the variation of silver layer thickness in quasi-TM mode, and **(iii)** loss spectra for the variation of silver layer thickness in quasi-TE mode. Reprinted with permission from SPIE [122]. **c(i)** Cross-sectional view of the PCF sensor with elliptical air holes, and **(ii)** loss spectra for the variation of analyte refractive index. Reprinted with permission from Optical Society of America [50]. **d(i)** Cross-sectional view of the PCF sensor with four microfluidic channels, and **(ii)** optical field distribution of the fundamental mode. Reprinted with permission from Springer [118]

of the PCF with high confinement loss exhibits fast decay. As a result, it will be difficult to obtain measurable signal at the output end.

The PCF SPR sensor proposed by Otupiri et al. consists of elliptical air holes and four microfluidic channels [50], which can detect multi-analytes having different refractive indices (see Fig. 9.5c(i)). The designed sensor can be used as the self-referencing mode making it suitable for eliminating external perturbations such as temperature variations, instrumental noises. The confinement losses for two different channels are shown in Fig. 9.5c(ii). It is reported that maximum wavelength sensitivity of 4600 nm/RIU and amplitude sensitivity of 425 RIU^{-1} can be obtained at gold layer thickness of 50 nm. A single ring hexagonal PCF sensor with four microfluidic channels has been demonstrated, where four modes are separately studied for multi-analyte detections (see Fig. 9.5d(i)) [118]. The birefringence property is used that exhibits different effective refractive indices for *x*-polarized and *y*-polarized modes. Due to this fact, one of the fundamental modes (either *x*- or *y*-polarized mode) shows higher confinement loss. The mode field distribution of the fundamental *y*-polarized HE_{11} mode is shown in Fig. 9.5d(ii). The proposed sensor shows maximum wavelength sensitivity of 2400 nm/RIU in *y*-polarized HE_{11} mode. Based on the birefringence property, another slotted PCF sensor has been proposed showing maximum wavelength sensitivity of 2000 nm/RIU and 1700 nm/RIU in *x*-polarized HE_{11} mode and *y*-polarized HE_{11} mode, respectively. In addition to multi-analytes detection, this slotted PCF sensor can be used for the detection of bulk and surface sensitivities.

9.5.2.2 D-Shaped PCF SPR Sensors

Recently, D-shaped PCF sensors have attracted much attention due to its definite advantages over other externally metal-coated sensors. In D-shaped PCF sensor, the top of the cladding is etched out in order to obtain a flat surface. Both the plasmonic material and analyte sample are placed on that flat surface. Most of the internally and externally metal-coated PCF sensors are based on the metal coating on the circular surface. In general, obtaining a uniform circular surface is difficult since it associates with unwanted surface roughness. Taking advantage from the flat surface, D-shaped PCF sensors provide possibilities for homogeneous coating with minimal surface roughness [123]. The unknown analyte can be detected by simply flowing on the flat surface. Moreover, plasmonic materials are deposited near to the core resulting in strong interaction of the core-guided mode and SPP mode. Due to such strong coupling, D-shaped PCF sensors show comparatively higher sensitivity than other PCF sensors. Currently, several D-shaped PCF sensors have been explored in order to enhance the performance [46, 47, 124–130]. Very recently, a D-shaped PCF sensor has been proposed using gold as the plasmonic material and titanium dioxide (TiO_2) for shifting the resonance wavelength from visible to near-infrared (see Fig. 9.6a(i)) [123]. Since plasmonic gold is deposited near the core, the evanescent field can easily reach to the metal surface. The electric field distributions of the fundamental core-guided mode and SPP mode are also shown in

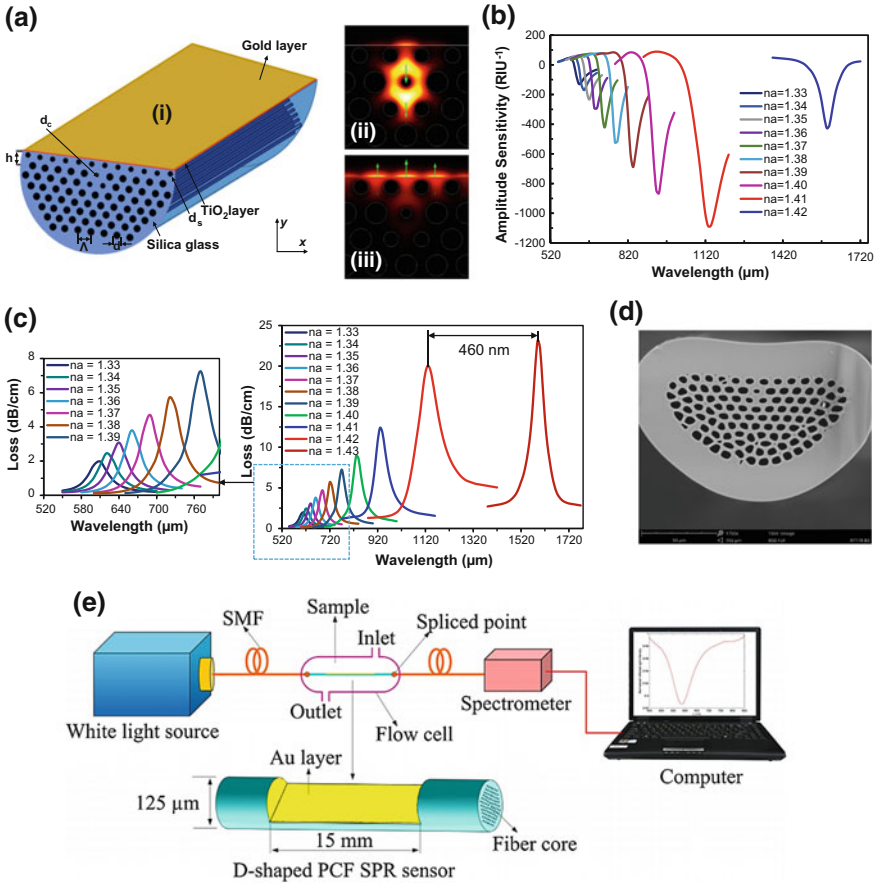

Fig. 9.6 **a(i)** 3D view of the D-shaped PCF sensor, **(ii)** electric field distribution of the fundamental core-guided mode, and **(iii)** electric field distribution of the SPP mode. **b** Amplitude sensitivity for the variation of analyte refractive index from 1.33 to 1.42. **c** Loss spectra for the variation of analyte refractive index from 1.33 to 1.43. **d** SEM image of the D-shaped PCF. **e** Generalized sensing setup using the D-shaped PCF. Reprinted with permission from IEEE [123]

Fig. 9.6a(ii)–(iii). In the sensing range between 1.33 and 1.43, the D-shaped sensor shows maximum amplitude sensitivity of 1086 RIU^{-1} (Fig. 9.6b) with sensing resolution of 9.2 $\times$ 10^{-6} RIU. It is also reported that maximum resonance wavelength shift of 460 nm can be obtained when analyte refractive index is varied from 1.42 to 1.43 (Fig. 9.6c).

The reported theoretical wavelength sensitivity and resolution are 46,000 nm/RIU and 2.2 $\times$ 10^{-6} RIU, respectively. The SEM image of the proposed D-shaped is shown in Fig. 9.6d. The general setup for detecting unknown analytes using D-shaped PCF is shown in Fig. 9.6e. Broadband white light source can be used to couple input light to the D-shaped PCF through a SMF. An analyte flow cell is

maintained on the flat surface region. The inlet and outlet of the flow cell can be obtained through a pump. The output light is again coupled to the SMF. The spectrometer is used to observe the output obtained from the SMF.

The hollow-core D-shaped PCF has been experimentally demonstrated having average wavelength sensitivity of 2336.2 nm/RIU [131] (see Fig. 9.7a(i)). The optical field distribution of the hollow-core D-shaped sensor is shown in Fig. 9.7a (ii). Compared to exposed core PCF sensor, this sensor shows higher sensitivity. Normalized light intensity of the proposed sensor due to the change of analyte refractive index is shown in Fig. 9.7a(iii). Due to structural simplicity, this sensor is convenient and suitable for practical sensing applications. The D-shaped PCF sensor proposed by Luan et al. can be potentially used for fast response and distributed sensing (see Fig. 9.7b(i)) [128]. The performance of this sensor has been

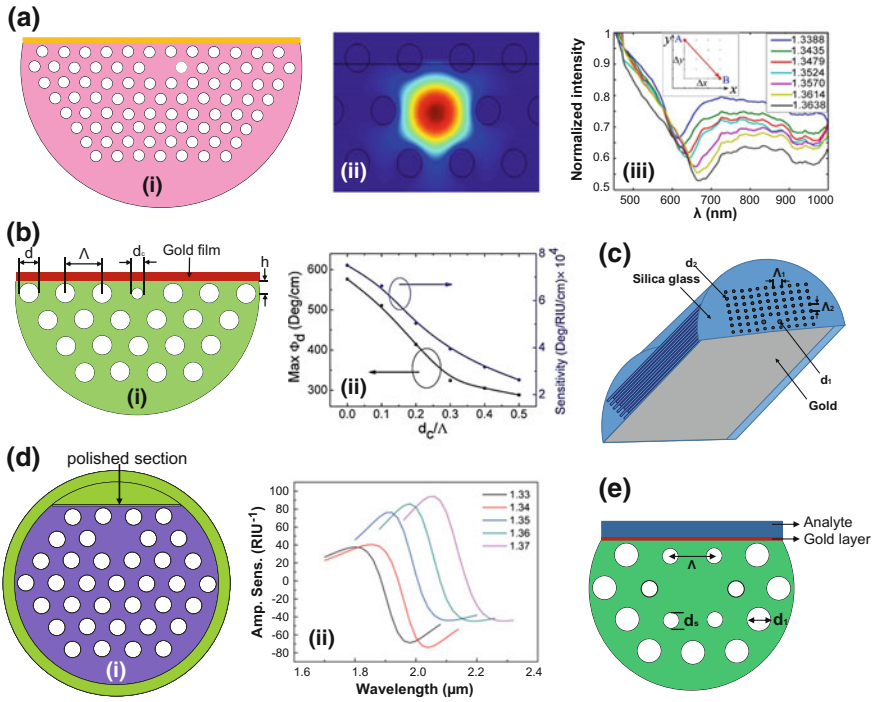

Fig. 9.7 D-shaped PCF SPR sensors. **a(i)** Cross-sectional view of the hollow-core D-shaped PCF sensor, **(ii)** optical field distribution of the fundamental mode, **(iii)** normalized intensity for different analyte refractive index [131]. **b(i)** Cross-sectional view of the D-shaped PCF sensor with external gold coating, **(ii)** variations of phase sensitivity and wavelength sensitivity due to the change of d_c/Λ. Reprinted with permission from Optical Society of America [128]. **c** Cross-sectional view of the D-shaped PCF with rectangular lattice air holes [46]. **d(i)** Cross-sectional view of the quasi-D-shaped PCF sensor and **(ii)** amplitude sensitivity for the variation of analyte refractive index from 1.33 to 1.37. Reprinted with permission from IEEE [132]. **e** Cross-sectional view of the hollow-core D-shaped PCF sensor with hexagonal lattice. Reprinted with permission from Springer [133]

demonstrated using wavelength, amplitude, and phase sensitivity. Variations of phase sensitivity and wavelength sensitivity due to the change of d_c/Λ are shown in Fig. 9.7b(ii). When the analyte refractive index is changed from 1.33 to 1.34, it shows wavelength sensitivity of 2900 nm/RIU, amplitude sensitivity of 120 RIU^{-1}, and phase sensitivity of 50,300 deg/RIU/cm. Another D-shaped PCF has been proposed having rectangular lattice air holes (see Fig. 9.7c) [46]. Two larger air holes are placed near the core to create birefringence in the structure resulting in higher FOM about 478.3 RIU^{-1}. Very recently, a quasi-D-shaped PCF SPR sensor has been proposed by An et al. using graphene and indium tin oxide (ITO) layers operating in the near-infrared wavelengths (see Fig. 9.7d(i)) [132]. In contrast to other D-shaped PCFs, this PCF structure is comparatively simple and easy to fabricate due to smaller polishing section. Moreover, it shows comparatively lower confinement loss than that of reported in other PCFs. Due to low confinement losses, the length of sensor can be enlarged making it suitable for remote sensing applications. Simulation results show maximum wavelength sensitivity of 10,693 nm/RIU and amplitude sensitivity of 95 RIU^{-1} at analyte refractive index of 1.37. The hollow-core D-shaped PCF sensor has been proposed using ITO as the plasmonic material [134]. This PCF also uses birefringence effect by employing two larger air holes near the core. It shows maximum wavelength sensitivity of 6000 nm/RIU, amplitude sensitivity of 148 RIU^{-1}, and phase sensitivity of 1.2×10^6 deg/RIU/cm. Besides, the D-shaped PCF has been proposed (see Fig. 9.7e) showing high average wavelength sensitivity of 7700 nm/RIU and resolution of 1.30×10^{-5} RIU [133]. Although D-shaped PCF sensors provide high sensitivity and eliminate the issue of uniform thickness, it requires accurate polishing of the predefined section. Moreover, few D-shaped PCF sensors show high confinement loss to polish out the upper air holes [46, 128, 133]. The high confinement loss potentially reduces the sensor length making them unsuitable for remote sensing applications.

9.5.2.3 Improved External Approach of PCF SPR Sensors

The improved PCF SPR sensors can be realized by putting plasmonic material and sensing medium outside the PCF structure. To date, several PCF sensors have been proposed based on improved external approach [37, 44, 109, 135–139]. The multi-core flat fiber (MCFF)-based PCF has been proposed (see Fig. 9.8a), where gold, TiO_2, and sensing layers are sequentially employed [109]. The MCFF operates in the near-infrared region and can be used to detect analyte having high refractive index from 1.46 to 1.48. This PCF provides easier fabrication since gold and TiO_2 layers are placed outside the PCF structure. Moreover, it requires coating of the flat surface rather than the circular one. The phase-matching condition and mode field distribution of the fundamental mode and SPP mode are shown in Fig. 9.8b. Since core of the MCFF is close to the gold layer, it provides strong interaction between core-guided mode and SPP mode.

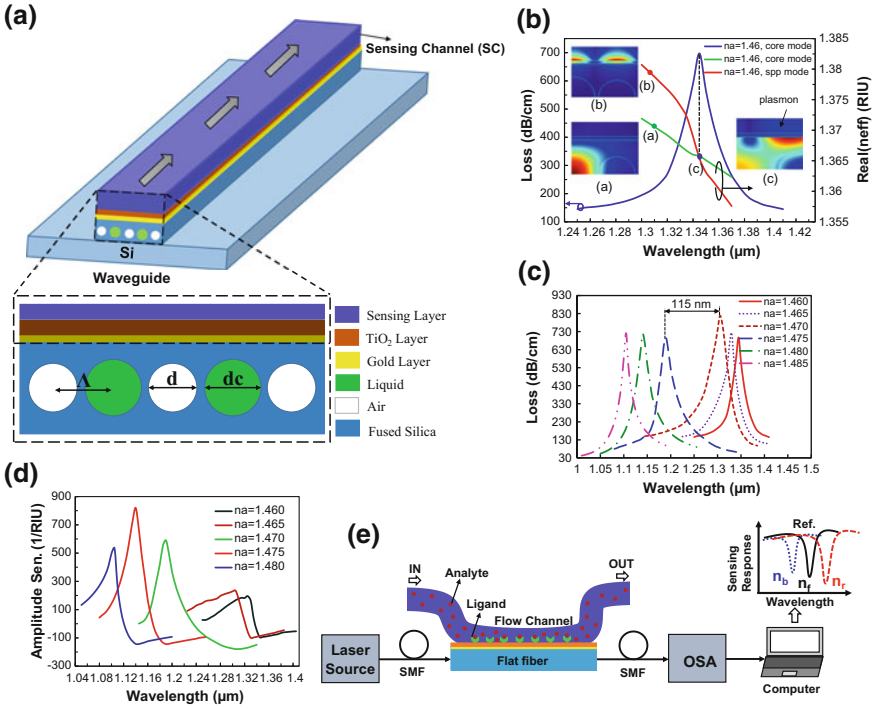

Fig. 9.8 **a** Schematic of the MCFF-based sensor. **b** Dispersion relation between core-guided mode and SPP mode with electric field distribution of the fundamental core-guided mode and SPP mode. **c** Loss spectra for the variation of analyte refractive index from 1.46 to 1.485. **d** Amplitude sensitivity for the variation of analyte refractive index from 1.46 to 1.485. **e** Generalized sensing setup using the MCFF. Reprinted with permission from Optical Society of America [109]

When the analyte refractive index is varied from 1.47 to 1.475, it shows maximum resonance wavelength shift of 115 nm (Fig. 9.8c). Amplitude sensitivity as a function of wavelength for the variation of analyte refractive index from 1.46 to 1.485 is shown in Fig. 9.8d. Simulation analysis shows maximum wavelength sensitivity of 23,000 nm/RIU and amplitude sensitivity of 820 RIU^{-1}. Due to fewer number of air holes, the proposed MCFF exhibits high confinement loss. The process of analyte flow through the sensing layer and typical sensing response is shown in Fig. 9.8e. Due to high linearity and very high sensitivity, the MCFF can be potentially used in high refractive index analyte detections.

Very recently, a hollow-core PCF SPR sensor has been reported in Fig. 9.9a(i) with maximum wavelength sensitivity of 4000 nm/RIU and amplitude sensitivity of 478 RIU^{-1} [140]. This PCF sensor eliminates major design issues due to its simple structure and minimum design parameters. It consists of hexagonal lattice cladding having four missing air holes in the second ring. The evanescent field produced from the core-guided mode penetrates through the missing air holes resulting in a strong interaction with metal surface as shown in Fig. 9.9a(ii)–(iii). The highest confinement loss for analyte refractive index of 1.37 is 60 dB/cm, and R^2 of 0.9868

are also demonstrated in Fig. 9.9a(iv). The proposed structure proposed by Liu et al. consists of seven air holes with annular analyte channel (Fig. 9.9b(i)) [141]. Due to fewer air holes in the cladding and smaller curved gold surface, fabrication of this sensor is comparatively easy. Moreover, perturbation with outer channel can be ignored since analyte channel is placed on the outermost layer. It is reported that wavelength sensitivity can be enhanced up to 7500 nm/RIU using extra graphene layer in the outer surface of the PCF. Variation of confinement loss with width of analyte channel for different operating wavelengths is shown in Fig. 9.9b(ii). The copper–graphene-based PCF sensor (see Fig. 9.9c(i)) shows average wavelength sensitivity of 2000 nm/RIU and amplitude sensitivity of 140 RIU^{-1} in the sensing range between 1.33 and 1.37 [136]. Two air holes in the cladding are scaled down in order to permit light propagating through their surrounding silica area. The scaled down air holes are kept close to the copper surface making intense interaction with evanescent field with metallic surface. The linear fitting of the resonance

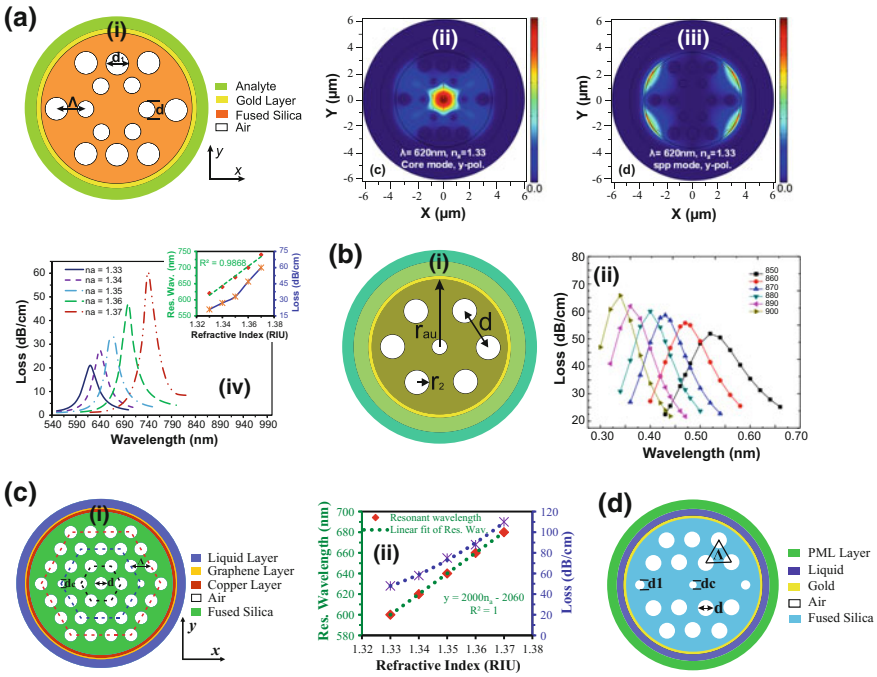

Fig. 9.9 Improved external approach of PCF SPR sensors. **a(i)** Cross-sectional view of the hollow-core PCF sensor, **(ii)** mode field distribution of the core-guided mode, **(iii)** mode field distribution of the SPP mode, and **(iv)** loss spectra for the variation of analyte refractive index from 1.33 to 1.37. Reprinted with permission from SPIE [140]. **b(i)** Cross-sectional view of the annular core PCF sensor and **(ii)** dependence of optical loss on the analyte channel width for different wavelengths [141]. **c(i)** Cross-sectional view of the copper–graphene-based PCF sensor and **(ii)** linear fitting of the resonance wavelengths. Reprinted with permission from IEEE [136]. **d** Cross-sectional view of the hexagonal lattice PCF sensor with external sensing. Reprinted with permission from IEEE [45]

Table 9.2 Performance comparison of the externally metal-coated PCF SPR sensors

References	Characteristics	RI range	Interrogation type	Sensitivity	Resolution (RIU)
[45]	Gold-coated PCF with external sensing approach	1.33–1.37	Wavelength	4000 nm/RIU	2.5×10^{-5}
			Amplitude	320 RIU^{-1}	3.125×10^{-5}
[50]	Multi-channel PCF with elliptical air holes	1.33–1.36	Wavelength	4600 nm/RIU	2.0×10^{-5}
			Amplitude	425 RIU^{-1}	2.0×10^{-5}
[109]	Multi-core flat fiber	1.46–1.485	Wavelength	23,000 nm/RIU	4.35×10^{-6}
			Amplitude	820 RIU^{-1}	1.22×10^{-5}
[118]	Four microfluidic slots	1.33–1.34	Wavelength	2400 nm/RIU	N/A
			Amplitude	N/A	N/A
[122]	Silver–gold bimetallic layer with multi-channels	1.33–1.35	Wavelength	4750 nm/RIU	2.1×10^{-5}
			Amplitude	1555 RIU^{-1}	6.43×10^{-6}
[123]	D-shaped fiber with gold deposited on titanium dioxide	1.33–1.43	Wavelength	46,000 nm/RIU	2.2×10^{-6}
			Amplitude	1086 RIU^{-1}	9.2×10^{-6}
[128]	Hollow-core D-shaped fiber	1.33–1.34	Wavelength	2900 nm/RIU	N/A
			Amplitude	120 RIU^{-1}	N/A
[132]	Quasi-D-shaped fiber with external graphene over ITO	1.33–1.38	Wavelength	10,693 nm/RIU	9.35×10^{-6}
			Amplitude	95 RIU^{-1}	1.05×10^{-4}
[134]	D-shaped PCF coated with indium tin oxide	1.28–1.34	Wavelength	6000 nm/RIU	1.6×10^{-7}
			Amplitude	148 RIU^{-1}	N/A
[136]	Copper–graphene-based PCF	1.33–1.37	Wavelength	2000 nm/RIU	5×10^{-5}
			Amplitude	140 RIU^{-1}	7.1×10^{-5}
[140]	Hollow-core PCF with external gold layer	1.33–1.37	Wavelength	4000 nm/RIU	2.5×10^{-5}
			Amplitude	478 RIU^{-1}	2.1×10^{-5}
[141]	PCF with annular analyte channel	1.38–1.42	Wavelength	7500 nm/RIU	1.33×10^{-5}
			Amplitude	513 RIU^{-1}	N/A

wavelength is shown in Fig. 9.9c(ii), where reported R^2 value is 1. Due to simple design and very high linearity, the proposed sensor has great potential for numerous sensing applications. Based on the birefringence effect, another simple PCF sensor has been demonstrated (Fig. 9.9d) having maximum wavelength sensitivity of 4000 nm/RIU and amplitude sensitivity of 320 RIU^{-1} [45]. Table 9.2 shows the performance comparison of the externally metal-coated PCF SPR sensors.

9.6 Future Directions

PCF-based SPR sensors are the key platform for numerous applications especially in biosensing, chemical sensing, and organic chemical sensing. All these sensing fields have potential opened area of research associated with PCF sensors. Although PCF SPR sensor is a topic of great interest, significant advancement has not been made from the point of device deployment. The major limitation of PCF SPR sensors is the fabrication challenges. Due to this fact, most of researches on PCF sensors are carried out by theoretical and simulation models. There are some experimental studies have been reported [52, 61, 115]; however, they are applicable for limited applications. Therefore, experimental investigation in order to use PCF sensors in practical applications can be a potential future work. Besides, detection of biological and biochemical analytes having wide range of refractive indices can be studied. PCF-based sensors are only implemented in laboratory-based experiments, which limit their capability for commercialization. A mobile analytical system can be developed in order to use it in field-based biosensing. Future progress of such systems can lead to highly robust, user-friendly, and compact PCF-based nanosensors.

One of the important challenges is to detect a particular molecule from a group of molecules. In general, a given system may contain undesirable molecules with similar properties. These unwanted molecules interact with the sensor causing false refractive index change. As a result, the performance of the sensor such as sensitivity, detection limit, and sensing resolution is greatly affected. The detection of the target molecules is problematic when the concentration of unwanted molecules is higher than that of target molecules. Another open issue of PCF SPR sensors is the effect of environmental perturbations such as temperature, humidity, vibration, and instrumental noise. These unwanted facts cause serious performance errors. Although few techniques have been developed to eliminate those issues, they are not matured enough [40, 142]. The current PCF sensors should be made consumers-friendly by fabricating them with simple and low-cost method. The PCF sensors should be able to reduce the test costs and rapid detections of unknown analytes.

The key challenge of PCF SPR sensors is the uniformity of the metal coating. In internally metal-coated PCF sensors, multiple air holes are selectively coated with plasmonic materials. From the fabrication point of view, it is really difficult to maintain uniform coating on selective air holes of the PCF. The externally

metal-coated PCF sensors require single metal coating, which is placed on the outer surface of the PCF. However, depositing metal on the circular surface creates huge surface roughness. Several physical methods such as vacuum evaporation [143], thermal evaporation [144], and RF sputtering [145] can be used for metal coating. Besides, several chemical methods such as chemical vapor deposition (CVD) [146], atomic layer deposition (ALD) [147], and wet-chemistry deposition [148] can be also used to deposit metal layer. However, none of these techniques provide guaranteed uniformity of the metal coating. These practical limitations are the main obstacles for employing PCF SPR sensors in practical applications. Few studies have been performed on Surface-Enhanced Raman Scattering (SERS) [149, 150], which is an important topic of metal nanoparticle-modified PCF. Research on SERS can be extended for the detection of low concentration without using fluorescent labeling. Moreover, SPR-like sensing technologies for THz frequencies are not matured. Several polymer materials such as TOPAS, HDPA, LDPA, and Teflon can be replaced by the silica background, and polaritonic materials can be used for THz sensing [100, 151].

9.7 Conclusions

In this chapter, recent advancements and challenges of PCF SPR sensors are reviewed and discussed. At first, we discuss the fundamentals of SPR and working mechanism of PCF SPR sensors. Then, we classify the PCF SPR sensors based on the location of plasmonic material deposition. Recently, results of internally metal-coated PCF SPR sensors are demonstrated and compared. We categorize the externally metal-coated PCF SPR sensors into three types: slotted PCF sensors, D-shaped PCF sensors, and improved PCF sensors. We also discuss and compare with recently proposed designs of these three categories. The study of SPR technique and PCF technology is the potential platform for level-free sensing. Progress on PCF SPR sensors is in initial stage; however, based on the experimental advancements achieved to date, PCF SPR can be regarded as an emerging sensing platform. In contrast to conventional prism-based SPR sensors, experimental setup of PCF-based sensors is relatively simple and cost-effective. Moreover, PCF SPR sensors have the potential to detect various types of biological and biochemical analytes. Although numerous simulation analyses have been performed on PCF SPR sensors, further experimental investigations are required for implementing them in practical applications such as medical diagnostics, food safety, and environmental monitoring.

References

1. C.E. Berger, J. Greve, Differential SPR immunosensing. Sens. Actuators B Chem. **63**, 103–108 (2000)
2. I. Stemmler, A. Brecht, G. Gauglitz, Compact surface plasmon resonance-transducers with spectral readout for biosensing applications. Sens. Actuators B Chem. **54**, 98–105 (1999)
3. Y. Fang, Label-free cell-based assays with optical biosensors in drug discovery. Assay Drug Dev. Technol. **4**, 583–595 (2006)
4. J. Homola, Surface plasmon resonance sensors for detection of chemical and biological species. Chem. Rev. **108**, 462–493 (2008)
5. R. Jorgenson, S. Yee, A fiber-optic chemical sensor based on surface plasmon resonance. Sens. Actuators B Chem. **12**, 213–220 (1993)
6. B.D. Gupta, R.K. Verma, Surface plasmon resonance-based fiber optic sensors: principle, probe designs, and some applications. J. Sens. **2009** (2009)
7. B. Lee, S. Roh, J. Park, Current status of micro-and nano-structured optical fiber sensors. Opt. Fiber Technol. **15**, 209–221 (2009)
8. C. Mouvet, R. Harris, C. Maciag, B. Luff, J. Wilkinson, J. Piehler et al., Determination of simazine in water samples by waveguide surface plasmon resonance. Anal. Chim. Acta **338**, 109–117 (1997)
9. C.P. Cahill, K.S. Johnston, S.S. Yee, A surface plasmon resonance sensor probe based on retro-reflection. Sens. Actuators B Chem. **45**, 161–166 (1997)
10. Y.-C. Cheng, W.-K. Su, J.-H. Liou, Application of a liquid sensor based on surface plasma wave excitation to distinguish methyl alcohol from ethyl alcohol. Opt. Eng. **39**, 311–314 (2000)
11. J. Homola, J. Dostálek, S. Chen, A. Rasooly, S. Jiang, S.S. Yee, Spectral surface plasmon resonance biosensor for detection of staphylococcal enterotoxin B in milk. Int. J. Food Microbiol. **75**, 61–69 (2002)
12. V. Koubová, E. Brynda, L. Karasová, J. Škvor, J. Homola, J. Dostálek et al., Detection of foodborne pathogens using surface plasmon resonance biosensors. Sens. Actuators B Chem. **74**, 100–105 (2001)
13. A. Nooke, U. Beck, A. Hertwig, A. Krause, H. Krüger, V. Lohse et al., On the application of gold based SPR sensors for the detection of hazardous gases. Sens. Actuators B Chem. **149**, 194–198 (2010)
14. B. Liedberg, C. Nylander, I. Lunström, Surface plasmon resonance for gas detection and biosensing. Sens. Actuators **4**, 299–304 (1983)
15. G. Ashwell, M. Roberts, Highly selective surface plasmon resonance sensor for NO2. Electron. Lett. **32**, 2089–2091 (1996)
16. M. Niggemann, A. Katerkamp, M. Pellmann, P. Bolsmann, J. Reinbold, K. Cammann, Remote sensing of tetrachloroethene with a micro-fibre optical gas sensor based on surface plasmon resonance spectroscopy. Sensors and Actuators B: Chemical **34**, 328–333 (1996)
17. P.J. Kajenski, Tunable optical filter using long-range surface plasmons. Opt. Eng. **36**, 1537–1541 (1997)
18. Y. Wang, Voltage-induced color-selective absorption with surface plasmons. Appl. Phys. Lett. **67**, 2759–2761 (1995)
19. J.S. Schildkraut, Long-range surface plasmon electrooptic modulator. Appl. Opt. **27**, 4587–4590 (1988)
20. G.T. Sincerbox, J.C. Gordon, Small fast large-aperture light modulator using attenuated total reflection. Appl. Opt. **20**, 1491–1496 (1981)
21. K.S. Johnston, S.R. Karlsen, C.C. Jung, S.S. Yee, New analytical technique for characterization of thin films using surface plasmon resonance. Mater. Chem. Phys. **42**, 242–246 (1995)
22. T. Akimoto, S. Sasaki, K. Ikebukuro, I. Karube, Refractive-index and thickness sensitivity in surface plasmon resonance spectroscopy. Appl. Opt. **38**, 4058–4064 (1999)

23. Y.-D. Su, S.-J. Chen, T.-L. Yeh, Common-path phase-shift interferometry surface plasmon resonance imaging system. Opt. Lett. **30**, 1488–1490 (2005)
24. L. Wang, R.J.H. Ng, S. Safari Dinachali, M. Jalali, Y. Yu, J.K. Yang, Large area plasmonic color palettes with expanded gamut using colloidal self-assembly. ACS Photonics **3**, 627–633 (2016)
25. S.A. Maier, Plasmonics: The promise of highly integrated optical devices. IEEE J. Sel. Top. Quantum Electron. **12**, 1671–1677 (2006)
26. S.P. Burgos, H.W. Lee, E. Feigenbaum, R.M. Briggs, H.A. Atwater, Synthesis and characterization of plasmonic resonant guided wave networks. Nano Lett. **14**, 3284–3292 (2014)
27. J. Zenneck, Über die Fortpflanzung ebener elektromagnetischer Wellen längs einer ebenen Leiterfläche und ihre Beziehung zur drahtlosen Telegraphie. Ann. Phys. **328**, 846–866 (1907)
28. A. Sommerfeld, Über die Ausbreitung der Wellen in der drahtlosen Telegraphie. Ann. Phys. **333**, 665–736 (1909)
29. R. Ritchie, Plasma losses by fast electrons in thin films. Phys. Rev. **106**, 874 (1957)
30. E. Kretschmann, H. Raether, Radiative decay of non radiative surface plasmons excited by light. Zeitschrift für Naturforschung A **23**, 2135–2136 (1968)
31. A. Otto, Excitation of nonradiative surface plasma waves in silver by the method of frustrated total reflection. Zeitschrift für Physik **216**, 398–410 (1968)
32. M. Piliarik, J. Homola, Z. Manıková, J. Čtyroký, Surface plasmon resonance sensor based on a single-mode polarization-maintaining optical fiber. Sens. Actuators B Chem. **90**, 236–242 (2003)
33. D. Monzón-Hernández, J. Villatoro, High-resolution refractive index sensing by means of a multiple-peak surface plasmon resonance optical fiber sensor. Sens. Actuators B Chem. **115**, 227–231 (2006)
34. D. Monzón-Hernández, J. Villatoro, D. Talavera, D. Luna-Moreno, Optical-fiber surface-plasmon resonance sensor with multiple resonance peaks. Appl. Opt. **43**, 1216–1220 (2004)
35. B. Gupta, A.K. Sharma, Sensitivity evaluation of a multi-layered surface plasmon resonance-based fiber optic sensor: a theoretical study. Sens. Actuators B Chem. **107**, 40–46 (2005)
36. M. Skorobogatiy, A.V. Kabashin, Photon crystal waveguide-based surface plasmon resonance biosensor. Appl. Phys. Lett. **89**, 143518 (2006)
37. B. Gauvreau, A. Hassani, M.F. Fehri, A. Kabashin, M. Skorobogatiy, Photonic bandgap fiber-based surface plasmon resonance sensors. Opt. Express **15**, 11413–11426 (2007)
38. A. Hassani, B. Gauvreau, M.F. Fehri, A. Kabashin, M. Skorobogatiy, Photonic crystal fiber and waveguide-based surface plasmon resonance sensors for application in the visible and near-IR. Electromagnetics **28**, 198–213 (2008)
39. Q. Wei, L. Shu-Guang, X. Jian-Rong, X. Xü-Jun, Z. Lei, Numerical analysis of a photonic crystal fiber based on two polarized modes for biosensing applications. Chin. Phys. B **22**, 074213 (2013)
40. B. Shuai, L. Xia, Y. Zhang, D. Liu, A multi-core holey fiber based plasmonic sensor with large detection range and high linearity. Opt. Express **20**, 5974–5986 (2012)
41. B. Shuai, L. Xia, D. Liu, Coexistence of positive and negative refractive index sensitivity in the liquid-core photonic crystal fiber based plasmonic sensor. Opt. Express **20**, 25858–25866 (2012)
42. A.A. Rifat, G.A. Mahdiraji, D.M. Chow, Y.G. Shee, R. Ahmed, F.R.M. Adikan, Photonic crystal fiber-based surface plasmon resonance sensor with selective analyte channels and graphene-silver deposited core. Sensors **15**, 11499–11510 (2015)
43. J.N. Dash, R. Jha, SPR biosensor based on polymer PCF coated with conducting metal oxide. IEEE Photonics Technol. Lett. **26**, 595–598 (2014)
44. J.N. Dash, R. Jha, Graphene-based birefringent photonic crystal fiber sensor using surface plasmon resonance. IEEE Photonics Technol. Lett. **26**, 1092–1095 (2014)

45. A. Rifat, G.A. Mahdiraji, Y. Sua, Y. Shee, R. Ahmed, D.M. Chow et al., Surface plasmon resonance photonic crystal fiber biosensor: a practical sensing approach. IEEE Photon. Technol. Lett. **27**, 1628–1631 (2015)
46. L. Peng, F. Shi, G. Zhou, S. Ge, Z. Hou, C. Xia, A surface plasmon biosensor based on a D-shaped microstructured optical fiber with rectangular lattice. IEEE Photonics J. **7**, 1–9 (2015)
47. F. Shi, L. Peng, G. Zhou, X. Cang, Z. Hou, C. Xia, An elliptical core D-shaped photonic crystal fiber-based plasmonic sensor at upper detection limit. Plasmonics **10**, 1263–1268 (2015)
48. A.K. Mishra, S.K. Mishra, B.D. Gupta, SPR based fiber optic sensor for refractive index sensing with enhanced detection accuracy and figure of merit in visible region. Opt. Commun. **344**, 86–91 (2015)
49. Q. Liu, S. Li, H. Chen, J. Li, Z. Fan, High-sensitivity plasmonic temperature sensor based on photonic crystal fiber coated with nanoscale gold film. Appl. Phys. Express **8**, 046701 (2015)
50. R. Otupiri, E.K. Akowuah, S. Haxha, Multi-channel SPR biosensor based on PCF for multi-analyte sensing applications. Opt. Express **23**, 15716–15727 (2015)
51. Y. Zhao, Z.-Q. Deng, J. Li, Photonic crystal fiber based surface plasmon resonance chemical sensors. Sens. Actuators B Chem. **202**, 557–567 (2014)
52. X. Yang, Y. Lu, M. Wang, J. Yao, A photonic crystal fiber glucose sensor filled with silver nanowires. Opt. Commun. **359**, 279–284 (2016)
53. J.N. Dash, R. Jha, Highly sensitive D shaped PCF sensor based on SPR for near IR. Opt. Quantum Electron. **48**, 137 (2016)
54. M.F.O. Hameed, M.Y. Azab, A. Heikal, S.M. El-Hefnawy, S. Obayya, Highly sensitive plasmonic photonic crystal temperature sensor filled with liquid crystal. IEEE Photonics Technol. Lett. **28**, 59–62 (2016)
55. C. Liu, F. Wang, J. Lv, T. Sun, Q. Liu, C. Fu et al., A highly temperature-sensitive photonic crystal fiber based on surface plasmon resonance. Opt. Commun. **359**, 378–382 (2016)
56. S. Singh, S.K. Mishra, B.D. Gupta, Sensitivity enhancement of a surface plasmon resonance based fibre optic refractive index sensor utilizing an additional layer of oxides. Sens. Actuators A **193**, 136–140 (2013)
57. M.R. Hasan, M.I. Hasan, M.S. Anower, Tellurite glass defect-core spiral photonic crystal fiber with low loss and large negative flattened dispersion over S + C + L + U wavelength bands. Appl. Opt. **54**, 9456–9461 (2015)
58. M.R. Hasan, M.S. Anower, M.I. Hasan, A Polarization Maintaining Single-Mode Photonic Crystal Fiber for Residual Dispersion Compensation. IEEE Photonics Technol. Lett. **28**, 1782–1785 (2016)
59. M.R. Hasan, M.S. Anower, M.I. Hasan, Polarization maintaining highly nonlinear photonic crystal fiber with closely lying two zero dispersion wavelengths. Opt. Eng. **55**, 056107–056107 (2016)
60. R. Ahmmed, R. Ahmed, S.A. Razzak, Design of large negative dispersion and modal analysis for hexagonal, square, FCC and BCC photonic crystal fibers, in *2013 International Conference on Informatics, Electronics & Vision (ICIEV)* (2013), pp. 1–6
61. A.A. Rifat, R. Ahmed, A.K. Yetisen, H. Butt, A. Sabouri, G.A. Mahdiraji et al., Photonic crystal fiber based plasmonic sensors. Sens. Actuators B Chem. **243**, 311–325 (2017)
62. J. Homola, Present and future of surface plasmon resonance biosensors. Anal. Bioanal. Chem. **377**, 528–539 (2003)
63. J. Homola, Electromagnetic theory of surface plasmons, in *Surface plasmon resonance based sensors* (2006), pp. 3–44
64. A.K. Sharma, R. Jha, B. Gupta, Fiber-optic sensors based on surface plasmon resonance: a comprehensive review. IEEE Sens. J. **7**, 1118–1129 (2007)
65. K.M. McPeak, S.V. Jayanti, S.J. Kress, S. Meyer, S. Iotti, A. Rossinelli et al., Plasmonic films can easily be better: rules and recipes. ACS Photonics **2**, 326–333 (2015)

66. T. Wieduwilt, A. Tuniz, S. Linzen, S. Goerke, J. Dellith, U. Hübner et al., Ultrathin niobium nanofilms on fiber optical tapers–a new route towards low-loss hybrid plasmonic modes. Sci. Rep. **5** (2015)
67. P.B. Johnson, R.-W. Christy, Optical constants of the noble metals. Phys. Rev. B **6**, 4370 (1972)
68. G.V. Naik, V.M. Shalaev, A. Boltasseva, Alternative plasmonic materials: beyond gold and silver. Adv. Mater. **25**, 3264–3294 (2013)
69. S.A. Zynio, A.V. Samoylov, E.R. Surovtseva, V.M. Mirsky, Y.M. Shirshov, Bimetallic layers increase sensitivity of affinity sensors based on surface plasmon resonance. Sensors **2**, 62–70 (2002)
70. N.D. Orf, O. Shapira, F. Sorin, S. Danto, M.A. Baldo, J.D. Joannopoulos et al., Fiber draw synthesis. Proc. Natl. Acad. Sci. **108**, 4743–4747 (2011)
71. M.A. Ordal, R.J. Bell, R.W. Alexander, L.L. Long, M.R. Querry, Optical properties of fourteen metals in the infrared and far infrared: Al, Co, Cu, Au, Fe, Pb, Mo, Ni, Pd, Pt, Ag, Ti, V, and W. Appl. Opt. **24**, 4493–4499 (1985)
72. P.G. Etchegoin, E. Le Ru, M. Meyer, Erratum: an analytic model for the optical properties of gold. J. Chem. Phys. **125**, 164705 (2006); J. Chem. Phys. **127**, 189901 (2007)
73. P.R. West, S. Ishii, G.V. Naik, N.K. Emani, V.M. Shalaev, A. Boltasseva, Searching for better plasmonic materials. Laser Photonics Rev. **4**, 795–808 (2010)
74. V. Kravets, R. Jalil, Y.-J. Kim, D. Ansell, D. Aznakayeva, B. Thackray et al., Graphene-protected copper and silver plasmonics. Sci. Rep. **4** (2014)
75. M. Schriver, W. Regan, W.J. Gannett, A.M. Zaniewski, M.F. Crommie, A. Zettl, Graphene as a long-term metal oxidation barrier: worse than nothing. ACS Nano **7**, 5763–5768 (2013)
76. M.M. Huq, C.-T. Hsieh, Z.-W. Lin, C.-Y. Yuan, One-step electrophoretic fabrication of a graphene and carbon nanotube-based scaffold for manganese-based pseudocapacitors. RSC Adv. **6**, 87961–87968 (2016)
77. I. Doron-Mor, Z. Barkay, N. Filip-Granit, A. Vaskevich, I. Rubinstein, Ultrathin gold island films on silanized glass. Morphology and optical properties. Chem. Mater. **16**, 3476–3483 (2004)
78. S. Szunerits, V.G. Praig, M. Manesse, R. Boukherroub, Gold island films on indium tin oxide for localized surface plasmon sensing. Nanotechnology **19**, 195712 (2008)
79. C. Granata, A. Vettoliere, M. Russo, B. Ruggiero, Noise theory of dc nano-SQUIDs based on Dayem nanobridges. Phys. Rev. B **84**, 224516 (2011)
80. A. Troeman, S. van der Ploeg, E. Il'Ichev, H.-G. Meyer, A. A. Golubov, M. Y. Kupriyanov et al., Temperature dependence measurements of the supercurrent-phase relationship in niobium nanobridges. Phys. Rev. B **77**, 024509 (2008)
81. M. Schmelz, Y. Matsui, R. Stolz, V. Zakosarenko, T. Schönau, S. Anders et al., Investigation of all niobium nano-SQUIDs based on sub-micrometer cross-type Josephson junctions. Supercond. Sci. Technol. **28**, 015004 (2014)
82. K. Sokhey, S. Rai, G. Lodha, Oxidation studies of niobium thin films at room temperature by X-ray reflectivity. Appl. Surf. Sci. **257**, 222–226 (2010)
83. S. Franzen, Surface plasmon polaritons and screened plasma absorption in indium tin oxide compared to silver and gold. J. Phys. Chem. C **112**, 6027–6032 (2008)
84. C. Rhodes, M. Cerruti, A. Efremenko, M. Losego, D. Aspnes, J.-P. Maria et al., Dependence of plasmon polaritons on the thickness of indium tin oxide thin films. J. Appl. Phys. **103**, 093108 (2008)
85. R.K. Verma, B.D. Gupta, Surface plasmon resonance based fiber optic sensor for the IR region using a conducting metal oxide film. JOSA A **27**, 846–851 (2010)
86. A. Tubb, F. Payne, R. Millington, C. Lowe, Single-mode optical fibre surface plasma wave chemical sensor. Sens. Actuators B Chem. **41**, 71–79 (1997)
87. W. Peng, S. Banerji, Y.-C. Kim, K.S. Booksh, Investigation of dual-channel fiber-optic surface plasmon resonance sensing for biological applications. Opt. Lett. **30**, 2988–2990 (2005)

88. Y. Zhang, C. Zhou, L. Xia, X. Yu, D. Liu, Wagon wheel fiber based multichannel plasmonic sensor. Opt. Express **19**, 22863–22873 (2011)
89. R. Verma, B. Gupta, Theoretical modelling of a bi-dimensional U-shaped surface plasmon resonance based fibre optic sensor for sensitivity enhancement. J. Phys. D Appl. Phys. **41**, 095106 (2008)
90. S.-F. Wang, M.-H. Chiu, R.-S. Chang, Numerical simulation of a D-type optical fiber sensor based on the Kretchmann's configuration and heterodyne interferometry. Sens. Actuators B Chem. **114**, 120–126 (2006)
91. Y.-C. Kim, W. Peng, S. Banerji, K.S. Booksh, Tapered fiber optic surface plasmon resonance sensor for analyses of vapor and liquid phases. Opt. Lett. **30**, 2218–2220 (2005)
92. M.-C. Navarrete, N. Díaz-Herrera, A. González-Cano, Ó. Esteban, Surface plasmon resonance in the visible region in sensors based on tapered optical fibers. Sens. Actuators B Chem. **190**, 881–885 (2014)
93. B. Špačková, J. Homola, Theoretical analysis of a fiber optic surface plasmon resonance sensor utilizing a Bragg grating. Opt. Express **17**, 23254–23264 (2009)
94. J. Zhao, S. Cao, C. Liao, Y. Wang, G. Wang, X. Xu et al., Surface plasmon resonance refractive sensor based on silver-coated side-polished fiber. Sens. Actuators B Chem. **230**, 206–211 (2016)
95. T.T. Nguyen, K.T.L. Trinh, W.J. Yoon, N.Y. Lee, H. Ju, Integration of a microfluidic polymerase chain reaction device and surface plasmon resonance fiber sensor into an inline all-in-one platform for pathogenic bacteria detection. Sens. Actuators B Chem. **242**, 1–8 (2017)
96. K. Bremer, B. Roth, Fibre optic surface plasmon resonance sensor system designed for smartphones. Opt. Express **23**, 17179–17184 (2015)
97. Y. Yuan, T. Guo, X. Qiu, J. Tang, Y. Huang, L. Zhuang et al., Electrochemical surface plasmon resonance fiber-optic sensor: in situ detection of electroactive biofilms. Anal. Chem. **88**, 7609–7616 (2016)
98. M.R. Hasan, S. Akter, T. Khatun, A.A. Rifat, M.S. Anower, Dual-hole unit-based kagome lattice microstructure fiber for low-loss and highly birefringent terahertz guidance. Opt. Eng. **56**, 043108–043108 (2017)
99. T.A. Birks, J.C. Knight, P.S.J. Russell, Endlessly single-mode photonic crystal fiber. Opt. Lett. **22**, 961–963 (1997)
100. M.R. Hasan, M.S. Anower, M.I. Hasan, S. Razzak, Polarization maintaining low-loss slotted core kagome lattice THz fiber. IEEE Photonics Technol. Lett. **28**, 1751–1754 (2016)
101. M.R. Hasan, M.A. Islam, A.A. Rifat, M.I. Hasan, A single-mode highly birefringent dispersion-compensating photonic crystal fiber using hybrid cladding. J. Mod. Opt. **64**, 218–225 (2017)
102. R. Slavík, J. Homola, J. Čtyroký, Single-mode optical fiber surface plasmon resonance sensor. Sens. Actuators B Chem. **54**, 74–79 (1999)
103. D. Gao, C. Guan, Y. Wen, X. Zhong, L. Yuan, Multi-hole fiber based surface plasmon resonance sensor operated at near-infrared wavelengths. Opt. Commun. **313**, 94–98 (2014)
104. W. Qin, S. Li, Y. Yao, X. Xin, J. Xue, Analyte-filled core self-calibration microstructured optical fiber based plasmonic sensor for detecting high refractive index aqueous analyte. Opt. Lasers Eng. **58**, 1–8 (2014)
105. Z. Fan, S. Li, Q. Liu, G. An, H. Chen, J. Li et al., High sensitivity of refractive index sensor based on analyte-filled photonic crystal fiber with surface plasmon resonance. IEEE Photonics J. **7**, 1–9 (2015)
106. X. Yu, Y. Zhang, S. Pan, P. Shum, M. Yan, Y. Leviatan et al., A selectively coated photonic crystal fiber based surface plasmon resonance sensor. J. Opt. **12**, 015005 (2009)
107. P. Bing, J. Yao, Y. Lu, Z. Li, A surface-plasmon-resonance sensor based on photonic-crystal-fiber with large size microfluidic channels. Opt. Appl **42**, 493–501 (2012)
108. W.L. Ng, A.A. Rifat, W.R. Wong, G. Mahdiraji, F.M. Adikan, A novel diamond ring fiber-based surface plasmon resonance sensor. Plasmonics, 1–6 (2017)

109. A.A. Rifat, G. Mahdiraji, Y.M. Sua, R. Ahmed, Y. Shee, F.M. Adikan, Highly sensitive multi-core flat fiber surface plasmon resonance refractive index sensor. Opt. Express **24**, 2485–2495 (2016)
110. X. Yang, Y. Lu, B. Liu, J. Yao, Analysis of graphene-based photonic crystal fiber sensor using birefringence and surface plasmon resonance. Plasmonics **12**, 489–496 (2017)
111. D. Li, W. Zhang, H. Liu, J. Hu, G. Zhou, High sensitivity refractive index sensor based on multicoating photonic crystal fiber with surface plasmon resonance at near-infrared wavelength. IEEE Photonics J. **9**, 1–8 (2017)
112. C. Liu, L. Yang, X. Lu, Q. Liu, F. Wang, J. Lv et al., Mid-infrared surface plasmon resonance sensor based on photonic crystal fibers. Opt. Express **25**, 14227–14237 (2017)
113. G. An, S. Li, X. Yan, X. Zhang, Z. Yuan, H. Wang et al., Extra-broad photonic crystal fiber refractive index sensor based on surface plasmon resonance. Plasmonics **12**, 465–471 (2017)
114. X. Fu, Y. Lu, X. Huang, J. Yao, Surface plasmon resonance sensor based on photonic crystal fiber filled with silver nanowires. Opt. Appl **41**, 941–951 (2011)
115. Y. Lu, M. Wang, C. Hao, Z. Zhao, J. Yao, Temperature sensing using photonic crystal fiber filled with silver nanowires and liquid. IEEE Photonics J. **6**, 1–7 (2014)
116. Y. Lu, X. Yang, M. Wang, J. Yao, Surface plasmon resonance sensor based on hollow-core PCFs filled with silver nanowires. Electron. Lett. **51**, 1675–1677 (2015)
117. N. Luan, J. Yao, A hollow-core photonic crystal fiber-based SPR sensor with large detection range. IEEE Photonics J. (2017)
118. S.I. Azzam, M.F.O. Hameed, R.E.A. Shehata, A. Heikal, S.S. Obayya, Multichannel photonic crystal fiber surface plasmon resonance based sensor. Opt. Quant. Electron. **48**, 142 (2016)
119. A. Hassani, M. Skorobogatiy, Photonic crystal fiber-based plasmonic sensors for the detection of biolayer thickness. J. Opt. Soc. Am. B **26**, 1550 (2009)
120. E.K. Akowuah, T. Gorman, H. Ademgil, S. Haxha, G.K. Robinson, J.V. Oliver, Numerical analysis of a photonic crystal fiber for biosensing applications. IEEE J. Quantum Electron. **48**, 1403–1410 (2012)
121. R. Otupiri, E. Akowuah, S. Haxha, H. Ademgil, F. AbdelMalek, A. Aggoun, A novel birefrigent photonic crystal fiber surface plasmon resonance biosensor. IEEE Photonics J. **6**, 1–11 (2014)
122. M.F.O. Hameed, Y.K. Alrayk, A.A. Shaalan, W.S. El Deeb, S.S. Obayya, Design of highly sensitive multichannel bimetallic photonic crystal fiber biosensor. J. Nanophotonics **10**, 046016–046016 (2016)
123. A.A. Rifat, R. Ahmed, G.A. Mahdiraji, F.M. Adikan, Highly sensitive d-shaped photonic crystal fiber-based plasmonic biosensor in visible to near-IR. IEEE Sens. J. **17**, 2776–2783 (2017)
124. M. Tian, P. Lu, L. Chen, C. Lv, D. Liu, All-solid D-shaped photonic fiber sensor based on surface plasmon resonance. Opt. Commun. **285**, 1550–1554 (2012)
125. Z. Tan, X. Li, Y. Chen, P. Fan, Improving the sensitivity of fiber surface plasmon resonance sensor by filling liquid in a hollow core photonic crystal fiber. Plasmonics **9**, 167–173 (2014)
126. J.N. Dash, R. Jha, On the performance of graphene-based D-shaped photonic crystal fibre biosensor using surface plasmon resonance. Plasmonics **10**, 1123–1131 (2015)
127. D.F. Santos, A. Guerreiro, J.M. Baptista, SPR microstructured D-type optical fiber sensor configuration for refractive index measurement. IEEE Sens. J. **15**, 5472–5477 (2015)
128. N. Luan, R. Wang, W. Lv, J. Yao, Surface plasmon resonance sensor based on D-shaped microstructured optical fiber with hollow core. Opt. Express **23**, 8576–8582 (2015)
129. Z. Fan, S. Li, H. Chen, Q. Liu, W. Zhang, G. An et al., Numerical analysis of polarization filter characteristics of D-shaped photonic crystal fiber based on surface plasmon resonance. Plasmonics **10**, 675–680 (2015)
130. Z. Tan, X. Hao, Y. Shao, Y. Chen, X. Li, P. Fan, Phase modulation and structural effects in a D-shaped all-solid photonic crystal fiber surface plasmon resonance sensor. Opt. Express **22**, 15049–15063 (2014)

131. Y. Chen, Q. Xie, X. Li, H. Zhou, X. Hong, Y. Geng, Experimental realization of D-shaped photonic crystal fiber SPR sensor. J. Phys. D Appl. Phys. **50**, 025101 (2016)
132. G. An, S. Li, H. Wang, X. Zhang, Metal Oxide-Graphene-Based Quasi-D-Shaped Optical Fiber Plasmonic Biosensor. IEEE Photonics J. **9**, 1–9 (2017)
133. R.K. Gangwar, V.K. Singh, Highly sensitive surface plasmon resonance based D-shaped photonic crystal fiber refractive index sensor. Plasmonics, 1–6 (2016)
134. T. Huang, Highly sensitive SPR sensor based on D-shaped photonic crystal fiber coated with indium tin oxide at near-infrared wavelength. Plasmonics **12**, 583–588 (2017)
135. X. Yang, Y. Lu, M. Wang, J. Yao, An exposed-core grapefruit fibers based surface plasmon resonance sensor. Sensors **15**, 17106–17114 (2015)
136. A.A. Rifat, G.A. Mahdiraji, R. Ahmed, D.M. Chow, Y. Sua, Y. Shee et al., Copper-graphene-based photonic crystal fiber plasmonic biosensor. IEEE Photonics J. **8**, 1–8 (2016)
137. V. Popescu, N. Puscas, G. Perrone, Power absorption efficiency of a new microstructured plasmon optical fiber. JOSA B **29**, 3039–3046 (2012)
138. V. Popescu, N. Puscas, G. Perrone, Strong power absorption in a new microstructured holey fiber-based plasmonic sensor. JOSA B **31**, 1062–1070 (2014)
139. A. Rifat, G.A. Mahdiraji, Y. Shee, M.J. Shawon, F.M. Adikan, A novel photonic crystal fiber biosensor using surface plasmon resonance. Proced. Eng. **140**, 1–7 (2016)
140. A.A. Rifat, M.R. Hasan, R. Ahmed, H. Butt, Photonic crystal fiber-based plasmonic biosensor with external sensing approach. J. Nanophotonics **12503**, 1 (2018)
141. C. Liu, L. Yang, W. Su, F. Wang, T. Sun, Q. Liu et al., Numerical analysis of a photonic crystal fiber based on a surface plasmon resonance sensor with an annular analyte channel. Opt. Commun. **382**, 162–166 (2017)
142. I.M. White, X. Fan, On the performance quantification of resonant refractive index sensors. Opt. Express **16**, 1020–1028 (2008)
143. R. Klenk, T. Walter, H.W. Schock, D. Cahen, A model for the successful growth of polycrystalline films of CuInSe2 by multisource physical vacuum evaporation. Adv. Mater. **5**, 114–119 (1993)
144. M.C. Barnes, D.-Y. Kim, H.S. Ahn, C.O. Lee, N.M. Hwang, Deposition mechanism of gold by thermal evaporation: approach by charged cluster model. J. Cryst. Growth **213**, 83–92 (2000)
145. L. Armelao, D. Barreca, G. Bottaro, G. Bruno, A. Gasparotto, M. Losurdo et al., RF-sputtering of gold on silica surfaces: evolution from clusters to continuous films. Mater. Sci. Eng., C **25**, 599–603 (2005)
146. P.J. Sazio, A. Amezcua-Correa, C.E. Finlayson, J.R. Hayes, T.J. Scheidemantel, N.F. Baril et al., Microstructured optical fibers as high-pressure microfluidic reactors. Science **311**, 1583–1586 (2006)
147. M.B. Griffiths, P.J. Pallister, D.J. Mandia, S.N.T. Barry, Atomic layer deposition of gold metal. Chem. Mater. **28**, 44–46 (2015)
148. J.A. Sioss, C.D. Keating, Batch preparation of linear Au and Ag nanoparticle chains via wet chemistry. Nano Lett. **5**, 1779–1783 (2005)
149. Z. Chen, Z. Dai, N. Chen, S. Liu, F. Pang, B. Lu et al., Gold nanoparticles-modified tapered fiber nanoprobe for remote SERS detection. IEEE Photonics Technol. Lett. **26**, 777–780 (2014)
150. M.K.K. Oo, Y. Han, R. Martini, S. Sukhishvili, H. Du, Forward-propagating surface-enhanced Raman scattering and intensity distribution in photonic crystal fiber with immobilized Ag nanoparticles. Opt. Lett. **34**, 968–970 (2009)
151. M.R. Hasan, M.A. Islam, M. Anower, S. Razzak, Low-loss and bend-insensitive terahertz fiber using a rhombic-shaped core. Appl. Opt. **55**, 8441–8447 (2016)